Nano Research

ISSN 1998-0124 CN 11-5974/O4
https://doi.org/10.1007/s12274-020-3087-z

Research Article

Atomistic modeling and rational design of optothermal tweezers for targeted applications

Hongru Ding[1], Pavana Siddhartha Kollipara[1], Linhan Lin[2] (✉), and Yuebing Zheng[1,3] (✉)

[1] *Walker Department of Mechanical Engineering, The University of Texas at Austin, Austin, TX 78712, USA*
[2] *State Key Laboratory of Precision Measurement Technology and Instruments, Department of Precision Instrument, Tsinghua University, Beijing 100084, China*
[3] *Materials Science & Engineering Program and Texas Materials Institute, The University of Texas at Austin, Austin, TX 78712, USA*

Received: 22 June 2020 / **Revised:** 22 August 2020 / **Accepted:** 3 September 2020

ABSTRACT

Optical manipulation of micro/nanoscale objects is of importance in life sciences, colloidal science, and nanotechnology. Optothermal tweezers exhibit superior manipulation capability at low optical intensity. However, our implicit understanding of the working mechanism has limited the further applications and innovations of optothermal tweezers. Herein, we present an atomistic view of opto-thermo-electro-mechanic coupling in optothermal tweezers, which enables us to rationally design the tweezers for optimum performance in targeted applications. Specifically, we have revealed that the non-uniform temperature distribution induces water polarization and charge separation, which creates the thermoelectric field dominating the optothermal trapping. We further design experiments to systematically verify our atomistic simulations. Guided by our new model, we develop new types of optothermal tweezers of high performance using low-concentrated electrolytes. Moreover, we demonstrate the use of new tweezers in opto-thermophoretic separation of colloidal particles of the same size based on the difference in their surface charge, which has been challenging for conventional optical tweezers. With the atomistic understanding that enables the performance optimization and function expansion, optothermal tweezers will further their impacts.

KEYWORDS

optothermal tweezers, optical tweezers, optical manipulation, thermophoresis, molecular dynamics simulation

1 Introduction

Contact-free manipulation of low-dimensional objects ranging from microscale to nanoscale plays an increasingly important role in biology, microfluidics, and colloidal science [1–4]. Optical tweezers have become one of the most versatile tools in the manipulation of tiny objects with different sizes, shapes, and materials [5–7]. However, the generation of optical gradient force relies on rigorous optics to create a tightly focused high-power laser beam, causing potential damage to fragile biological samples [8, 9]. Utilizing the enhanced gradient force in the vicinity of metallic nanoantennas, plasmonic tweezers were developed to trap nanoparticles at reduced laser power [10]. However, the inability of dynamic manipulation in plasmonic tweezers hinders their further applications [11]. To overcome these limitations, we have recently developed optothermal tweezers, i.e. opto-thermophoretic tweezers in non-electrolyte solvent and opto-thermoelectric tweezers in electrolyte solvent [12]. Taking advantages of the high-efficiency photon-to-phonon conversion and the directed particle migration along the temperature gradient, low-power (< 0.1 mW/μm^2) and dynamic optical manipulation of particles of different materials and sizes have been successfully demonstrated [13–16]. Beyond optical trapping, optothermal tweezers have proven to be a versatile tool in all-optical assembly [17] and printing [18] of nanoparticles, and have been exploited for a variety of applications such as digital manufacturing [19] and chiral sensing [20]. Despite the alluring perspective of optothermal tweezers, current theories on thermophoresis are limited or even contradictory in understanding the working principle of optothermal tweezers. For instance, in opto-thermophoretic tweezers, thermophoresis of colloids is attributed to the particle–solvent interactions altered by thermal expansion of solvent [21, 22]. Hydrophilic particles prefer to stay in the cold region where water density is higher, while hydrophobic particles stay in the hot region where water density is lower [22]. Nevertheless, Putnam pointed out that electric-double-layer-induced enthalpy change dominates the thermophoresis of colloids [23, 24]. In opto-thermoelectric tweezers, charge separation has proven critical to the thermoelectric response of the electrolyte solution [25, 26] and the thermal diffusion of the particles [27, 28]. However, most of the existing theoretical models oversimplify the contribution of charge separation, owing to a paucity of effective methods to study the charge separation at the atomistic level [29–32]. Recent experiments have revealed that the trapping force in optothermal tweezers is sensitive to a variety of parameters such as substrate, the surface charge of trapped objects, solute composition and environmental temperature, making it challenging to design optothermal tweezers of optimum performance for any targeted applications [14, 24, 33, 34].

Address correspondence to Linhan Lin, linlh2019@mail.tsinghua.edu.cn; Yuebing Zheng, zheng@austin.utexas.edu

Herein, we elaborate on the underlying mechanism of optothermal tweezers at the atomistic level by comprehensively studying the thermal response of ions and solvent molecules, and the resulted contribution to optothermal trapping forces. Our molecular dynamics (MD) simulations reveal that the thermoelectric field, which is induced by charge separation and water polarization, dominates the thermophoretic migration of the particles. This atomistic view is verified in our systematically designed experiments on opto-thermophoretic trapping of charged particles. Inspired by new sights provided by our atomistic model, we propose a general design guideline for optothermal tweezers. As a proof-of-concept, we optimize optothermal tweezers based on precise selection of salt and polymer solutions. Interestingly, high-performance optothermal tweezers can be achieved by choosing a proper electrolyte of extremely low concentration. Furthermore, we successfully achieve optical sorting of particles with different surface charges. Our fundamental understanding and design rule at atomic scale will lead to the further development and applications of optothermal tweezers in various areas such as nanoscience, colloidal sciences, and life sciences.

2 Thermophoretic trapping and repelling of charged polystyrene beads

Figure 1(a) illustrates the general concept of optothermal tweezers. A plasmonic substrate comprised of Au nanoislands (AuNIs, see Methods for the substrate fabrication) is irradiated by a focused 532 nm laser beam to excite localized surface plasmon for light-to-heat conversion. An appropriate temperature gradient (~ 10 K/μm) is generated via a low optical power of 0.06 mW/μm^2. Micro-/nanoparticles are trapped by a temperature gradient and confined at the laser spot. Successive optical images of an example of light-directed trapping process are shown in Fig. 1(b). A 2 μm polystyrene (PS) bead travels 10 μm in around 9 s and gets trapped at the laser spot. The drift velocity increases rapidly when the particle approaches the laser spot because of the non-uniform temperature gradient, and the velocity decreases to zero at the trapping position (Fig. 1(c)).

In order to understand the effect of solvent on the trapping force in the above-mentioned opto-thermophoretic trap, we examined the trapping behavior of PS beads with different surface charges in three different solutions: deionized (DI) water, sodium chloride (NaCl) (inorganic electrolyte) and cetyltrimethylammonium chloride (CTAC) (organic electrolyte) solutions, respectively. 2 μm PS beads with carboxyl (negatively charged) or aliphatic amine (positively charged) functional groups are selected as illustrative examples. As shown in Fig. 1(d), in DI water, negatively charged PS beads are trapped at the laser spot, while the positive beads are repelled. In contrast, negatively charged PS beads get repelled in NaCl solution, while positively charged particles get trapped. More interestingly, both PS beads are trapped at the laser spot in CTAC solution (see Movies ESM1–ESM6 for the real-time trapping behavior). We further quantified the mean drift velocity using the mean drift velocities measured when particles travel 10 μm towards/from the laser spot (Fig. 1(e)). Among them, CTAC solution exhibits the maximum mean drift velocity while NaCl solution shows the minimum one. From these trapping phenomena, we anticipate that the electrostatic force is critical in both opto-thermophoretic trapping (in water) and opto-thermoelectric trapping (in electrolyte solution).

3 Atomistic models of thermo-electro-mechanics in optothermal tweezers

In this section, based on the experiments (Figs. 1(d) and 1(e)) and MD simulations, we propose two models to explain the thermo-electro-mechanics in opto-thermophoretic and opto-thermoelectric trapping, respectively. For opto-thermophoretic

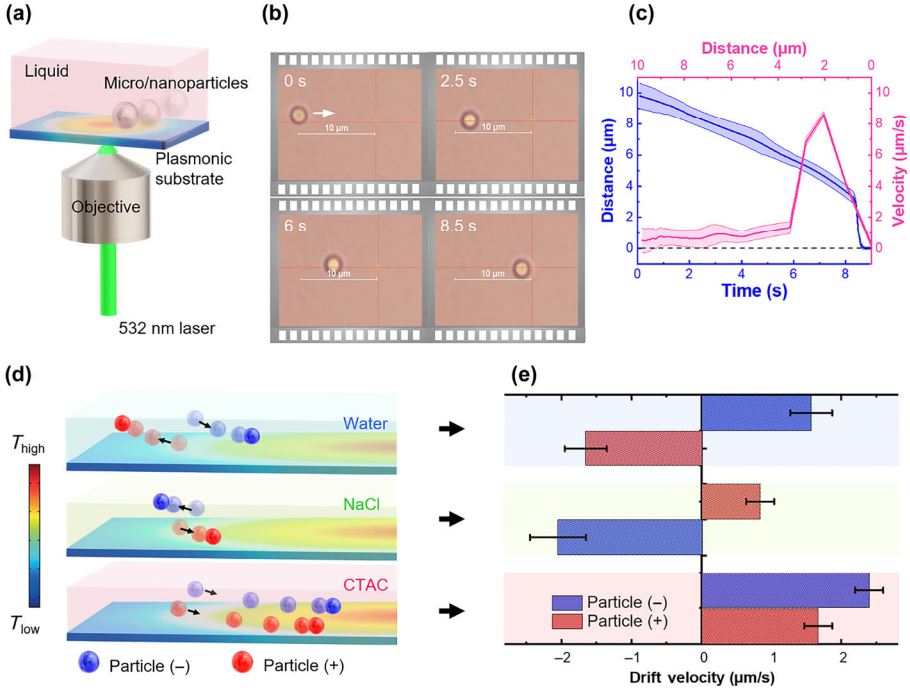

Figure 1 Opto-thermal manipulation of nanoparticles. (a) Schematic illustration of particle trapping. (b) Successive optical images of a representative trapping process (the cross marks the position of laser beam). (c) Position of PS beads versus time and drift velocity versus position profiles. The corresponding SD is indicated by shaded areas (the average values are obtained by processing eight individual videos). (d) Trapping or repelling of charged PS beads in water, NaCl and CTAC solution. Positively and negatively charged beads are repelled and trapped in water, respectively. A totally opposite phenomenon can be observed in NaCl solution. In CTAC solution, both beads are trapped. (e) Mean drift velocity in three liquids (negative velocity corresponds to repelling velocity).

tweezers, the trapping of PS beads is mainly determined by the sign of surface charge on the particles. Experiments on charged silicon and silica particles further verified this hypothesis (Movies ESM7 and ESM9). Intuitively, electrokinetic interactions between the particles and the solvent (i.e. water) play important role in determining the trapping capability. Owing to the strong electronegativity difference of oxygen and hydrogen, partial charges exist on individual atoms in a neutral water molecule (Fig. 2(a)). Unidirectional alignment of the polarized water under an external field results in an electric field [35]. Specifically, water molecule rotates and translates until the dipole moment aligns with the temperature gradient, as shown in Fig. 2(a). Such an arrangement of water molecules develops a thermoelectric (TE) field towards the cold region (blue arrows in Fig. 2(b)). Herein, we define TE field pointing towards the hot region as positive and TE field pointing away from the hot region as negative. Negative PS beads experience the negative TE field in water and travel from cold to hot and finally get trapped at the laser spot, while positive PS beads are repelled from the laser hotspot. This electric effect is similar to the mechanism of particle drift in optoelectronic tweezers [36, 37]. Since the two functional groups on PS beads are hydrophilic in nature, our observation is different from previously reported viewpoints that all hydrophilic particles are thermophobic [21, 22]. Further discussion on the effect of surface properties of particles will be shown in the next section.

For opto-thermoelectric tweezers, the primary trapping force is the thermoelectric force stemming from the free ions in the solution. It is known that considerable voltage can be induced by introducing a temperature gradient within an electrolyte solution [38]. Accordingly, a charged particle should move along (or opposite) the direction of TE field. In electrolyte solutions, TE field originates from the heat induced separation of cations and anions, and is proportional to the difference in Soret coefficient (S_T) of ions. To study the thermoelectric trapping capability of NaCl and CTAC solutions, we calculated S_T of different cations and anions via MD simulations (simulation details are shown in Methods). A temperature gradient is applied along Z axis of electrolyte solutions (Fig. 2(c)) and the ionic distribution at steady state is recorded to evaluate S_T of individual ions. The difference in S_T of cations and anions is written as $\Delta S_T = |S_T(\text{cation}) - S_T(\text{anion})|$, as shown in Fig. 2(d). As shown in Fig. 2(e), the cations (with larger S_T) diffuse farther away from the hot region than the anions, creating a positive TE field in the vicinity of the hot region. The insets of Fig. 2(c) show the spatial distribution of ions at steady state in CTAC and NaCl solutions. In NaCl solution, the ionic separation is almost invisible because of small ΔS_T. In contrast, the ionic separation is much more obvious in CTAC solution, while the CTAC molecules migrate to the cold region and the Cl^- ions stay at the hot region, which is consist with our model. Although water polarization also exists in electrolyte solutions, our simulations reveal that the intensity of TE_{water} is smaller than that of TE_{ions}, with an opposite sign (Fig. S2 in the Electronic Supplementary Material (ESM)). Hence, the total TE field remains positive and the positively charged particle can be trapped at the hot region.

To verify our models, TE field was calculated through the integration of charge density [26]

$$E(Z) = \frac{1}{\varepsilon_0}\int \rho(Z)\mathrm{d}Z$$

$$\rho = \sum_{i=1}^{N}\frac{\delta(Z - Z_i)q_i}{A} \quad (1)$$

where ε_0 is vacuum permittivity and $\rho(Z)$ is the charge density

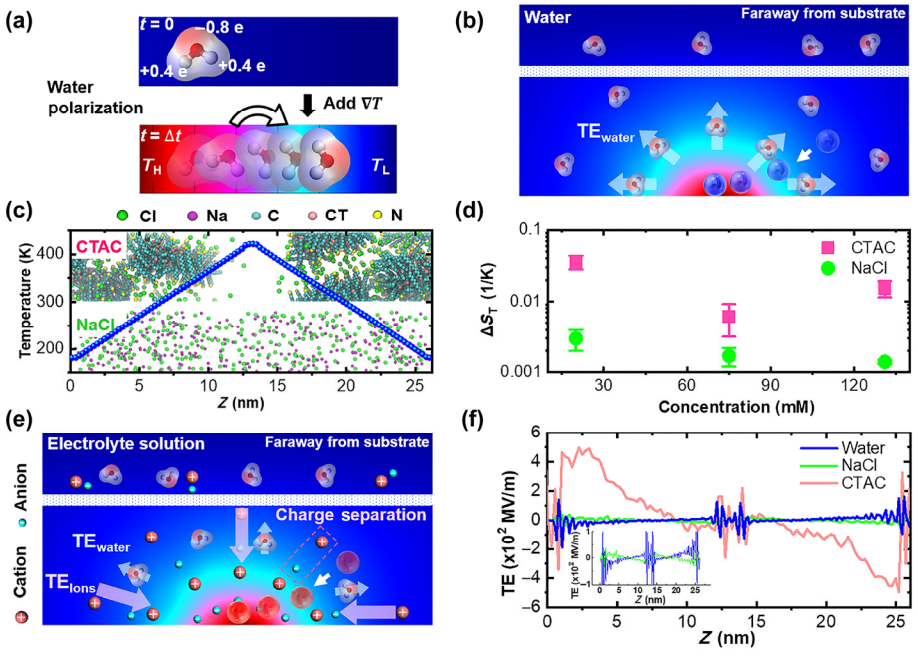

Figure 2 Atomistic view of optothermal tweezers. (a) Water molecule shows strong polarity: The charges of an oxygen atom and a hydrogen atom are roughly −0.8e and 0.4e, respectively. Water can be polarized by thermal gradient: Water molecules rotate and transport until oxygen and hydrogen atoms are aligned towards the cold and hot region, respectively. (b) The mechanism of opto-thermophoretic tweezers: Under a temperature gradient, water molecules are in a specific arrangement and generate an electric field toward cold region for negative particle trapping. In the region far away from the hot substrate, water molecules are randomly oriented. (c) Temperature gradient (blue dots) and ionic distribution (NaCl and CTAC solutions) at steady state obtained in MD simulations. Green, purple, cyan, pink and yellow spheres are chlorine, sodium, carbon, carbon (tail) and nitrogen (head) atoms, respectively. (d) Difference in the effective S_T between cations and anions (pink squares: CTAC, green dots: NaCl). (e) The mechanism of opto-thermoelectric tweezers: Under temperature gradient, cations diffuse father than anions. Such separation leads to an electric field toward the hot region for positive particle trapping. In the region far away from the hot substrate, water molecules and ions are in random order. Additionally, ions stay close with their counterions. (f) TE fields of water, NaCl (1 M) and CTAC (1 M). The highlighted areas represent the hot (red) and cold (blue) regions.

at Z, A is the area of XY plane of simulation box, q_i is the charge of oxygen or hydrogen atom for water polarization and ions for charge separation. The TE field profiles of three different solvents are shown in Fig. 2(f). Maximum electric field strength is observed in CTAC solution arising from the maximum value of ΔS_T(CTAC), while a minimum electric field strength is obtained in NaCl solution (inset of Fig. 2(f)). One should note that both charge separation and water polarization are taken into consideration for TE_{CTAC} and TE_{NaCl} in Fig. 2(f). The inhomogeneous electric field is induced by the proximity between hot and cold layers. We can see that the simulated TE fields in the three liquid systems can be verified by measured trapping velocities: $V_{trapping}$(CTAC) > $V_{trapping}$(water) > $V_{trapping}$(NaCl), which proves that the dominant trapping force of optothermal tweezers (opto-thermophoretic tweezers and opto-thermoelectric tweezers) arises from the TE field. The drift motion of particles can be understood as the electrophoresis of particles under the TE field [39] induced by a laser beam. It should be noted that the osmotic force has limited contribution (around 5%, see Note S3 in the ESM). The thermo-osmosis flow on the substrate is also ignorable here, because of the ionic substrate and relatively thicker chamber [40, 41].

In addition, trapping can be even more complicated in organic electrolyte solutions where the surface charge of particles can be modified by the adsorption of solutes. With the existence of alkane chain, organic ions usually possess stronger adsorption ability than inorganics [42], because of the hydrophobic interaction between organic ions with particles. In our experiments, CTA^+ ions show strong absorption ability, which turns the surface charge of PS beads from negative to positive. Afterward, the PS beads migrate along in the direction of TE_{CTAC} field. Future investigation on the effect of particles' surface property is essential for complete understanding.

4 Dominating factors of optothermal tweezers

To comprehensively understand the working principle of optothermal tweezers and design more versatile tweezers, we quantitatively analyze how the ionic concentration and surface properties of particles affect the optothermal trapping in this section. Firstly, we calculated TE fields in pure water and electrolyte solutions with different electrolyte concentrations (Fig. 3(a)). We can see that the magnitude of TE_{water} field is comparable to TE field of low ionic concentration (< 10 mM) in electrolyte solution due to the strong polarity of water. The considerable TE_{water} field explains the low-power trapping of polymer nanoparticles [34], lipid vesicles [16] and biological cells [15] in DI water. Moreover, the dependency of TE field on the ionic concentration is totally different between NaCl and CTAC. The TE field in NaCl solution shows a monotonic decrease with concentration because of the small difference in the effective S_T between Na^+ ions and Cl^- ions (see Fig. 2(d)). However, the TE field in CTAC solution decreases initially from 9.90 to 7.45 MV/m as concentration increases from 10 to 75 mM, and later increases to 132.68 MV/m as concentration increases to 1 M. The effective S_T of an ion can be expressed as [43]

$$S_T = S_T^* + \Delta S_T^{coupling}$$
$$\Delta S_T^{coupling} = -\frac{\nu_i \sum \nu_i C_i S_{Ti}^*}{\sum C_i} \quad (2)$$

where S_T^* is the intrinsic ionic Soret coefficient, $\Delta S_T^{coupling}$ is the change in Sorect coefficient induced by charge coupling, the subscript i indicates the ion species, ν is the sign of the ionic charge, and C is the ionic concentration. In dilute NaCl solution, ions show intrinsic thermal diffusion due to weak charge coupling: $S_T(Na^+) \approx S_T^*(Na^+) > S_T(Cl^-) \approx S_T^*(Cl^-)$. The magnitude of $\Delta S_T^{coupling}$ increases when the ionic concentration increases. For a type of ion with the higher S_T^* in any electrolyte solution, its $\Delta S_T^{coupling}$ is negative. Thereby, S_T decreases with concentration. Instead, for the ions with lower S_T^*, S_T is increased by the larger positive $\Delta S_T^{coupling}$. Therefore, in NaCl solution at high concentration, both ions have similar S_T and the charge separation becomes weaker, which results in a lower TE_{NaCl}.

In CTAC solution, similar to that of NaCl, the TE field decreases when the ionic concentration increases from 10 to 75 mM as $S_T(CTA^+) > S_T^*(Cl^-)$. However, above 75 mM, an unexpected increase of TE field is observed. To understand the physical mechanism, we study the charge separation of the CTAC molecules at different concentrations. Here, we use the local number fraction of cations and anions to describe charge separation (Fig. 3(b)). For zero charge separation, $\frac{n_+}{n_+ + n_-} = \frac{n_-}{n_+ + n_-} = 0.5$ at any position, where n_+ and n_- are volumetric number density of cations and anions. The value of $\left|\frac{n_+}{n_+ + n_-} - 0.5\right|$ represents the degree of charge separation in the system. As shown in the top panel of Fig. 3(b), at a CTAC concentration of 1 M, the value of $\frac{n_\pm}{n_+ + n_-}$ is always larger than that at 75 mM. According to Gauss law, the electric field $E = \int \rho dz/\varepsilon_0$, where ρ is charge density. The TE field can be

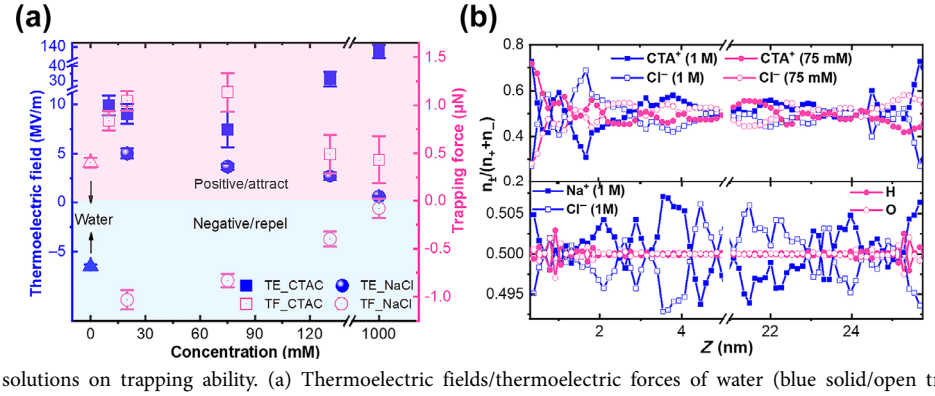

Figure 3 Effects of solutions on trapping ability. (a) Thermoelectric fields/thermoelectric forces of water (blue solid/open triangles), NaCl (green solid/open pentagons) and CTAC (pink solid/open squares) solutions at different concentrations. (b) Charge separation of 1 M and 75 mM CTAC solutions (top panel) and 1 M NaCl solution (bottom panel). The separation of oxygen and hydrogen atoms (water polarization) in pure water (bottom). n_+ (n_-) is local number fraction of cations (anions). Note that the vertical axis of the bottom panel is much smaller than the top one.

written as

$$E = \frac{\int e\left(\frac{n_+ - n_-}{n_+ + n_-}\right)(n_+ + n_-)\mathrm{d}z}{\varepsilon_0} \quad (3)$$

Therefore, the more $\left|\frac{n_\pm}{n_+ + n_-}\right|$ deviates from 0.5, the higher TE field comes into being. To explain the larger S_T of CTA^+ micelles at high concentration, we simulated the formation of micelles in CTAC solution at different concentrations and observed an increasing aggregation number of CTA^+ ions at higher concentration (see Fig. S2 in the ESM). Larger polymer molecules usually possess higher S_T, therefore, thermal diffusion of CTA^+ micelles is enhanced at higher concentrations. S_T as a function of CTAC concentration shows a similar trend with TE_{CTAC} (Fig. 2(d)), which further verifies the relationship among TE field, charge separation, Soret coefficient and micelle size. A significantly smaller charge separation of NaCl solution is observed in the bottom panel of Fig. 3(b), as expected from TE fields. The charge separation as a function of ionic concentration is shown in Fig. S10 in the ESM. In water, the separation of oxygen atoms (negative) and hydrogen atoms (positive) is also given (bottom panel in Fig. 3(b)). The charge separation is much weaker than that in dissociated ions, because of the covalent bonding between oxygen and hydrogen atoms. But the spatial fluctuation frequency of charge separation is much higher than that in CTAC and NaCl solutions.

We further calculate the trapping forces (i.e. thermoelectric forces) in water, NaCl and CTAC solutions through integrating the product of charge density of PS beads and TE field along Z axis, as illustrated in Fig. 3(a). Herein, we ignore the effect induced by the spatial occupation of the beads on TE field, which is not significant as we discussed in our previous work [44]. However, for particles possessing significantly different thermal conductivity from that of water such as gold particles, the particle-occupation-induced distortion in the temperature field should not be ignored. Surface charge density σ is evaluated from the measured zeta potential ζ (see Fig. S9 in the ESM) of PS beads as [45]

$$\sigma = \frac{\varepsilon_r\varepsilon_0\kappa k_B T}{e}\left[\exp\left(\frac{e\zeta}{2k_BT}\right) - \exp\left(-\frac{e\zeta}{2k_BT}\right) - \frac{4}{\kappa a}\frac{\left(\exp\left(\frac{e\zeta}{2k_BT}\right)-1\right)}{\left(\exp\left(\frac{e\zeta}{2k_BT}\right)+1\right)}\right]$$

$$\kappa = \left(\frac{2ne^2}{\varepsilon_r\varepsilon_0 k_B T}\right)^{1/2} \quad (4)$$

where ε_r and ε_0 are relative and vacuum permittivity, κ is the inverse Debye length, a is the particle radius and n is electrolyte concentration. The surface charge density of dielectric particles in this work is assumed uniform, while the non-uniform surface charge density induced by the free movement of charges in conductive particles should not be ignored. We obtain the maximum trapping force in 20 mM CTAC solution. The repelling force in 20 mM NaCl solution is larger than the trapping force in water. We should note that the trapping force in water is smaller than the trapping/repelling force in CTAC/NaCl solution because the surface charge density of PS beads in water is lower than that in electrolyte solutions [46].

Beyond the ionic species and concentration, the properties of particle surface are also important to the trapping capability in optothermal tweezers, especially in organic electrolyte solutions. For example, the hydrophilicity of the particle surface significantly affects the adsorption of ions, which, in turn, changes the surface charge density. Herein, opto-thermal trapping of hydrophobic and hydrophilic particles is studied experimentally and numerically to understand the adsorption effect. We chose 1 μm silicon (Si) and silicon dioxide (SiO_2) particles because of their similar density (Si: 2.32 g/cm^3; SiO_2: 2.65 g/cm^3) but different hydrophilicity (water contact angle: ~ 90° (Si); ~ 0° (SiO_2)) [47]. First, the adsorption of CTAC on the surface of Si and SiO_2 particles was simulated. As shown in Fig. 4(a), Si surface is fully covered by CTA^+ groups that align with the surface due to the hydrophobic attraction between Si atoms and alkane chains. Self-assembly of CTAC micelles is observed far away from the particle surface because the concentration is higher than the critical micellar concentration (~ 0.13 mM). Without water molecules, the distance between CTA^+ and Si surface is small, leading to tightly packed adsorption on the surface and turning neutral Si particles to positive particles. Since the TE_{CTAC} field is positive, the positive Si particles are attracted to the laser spot and get trapped (see Movie ESM9). Different from Si, the adsorption of CTAC on SiO_2 mainly relies on the electrostatic attraction between dissociated heat groups (SiO^-) with CTA^+ ions, whose head groups are positive. Thus, the alkane chains align with SiO_2 surface plane with small angles ($0° < \theta < 45°$), as shown in Fig. 4(b). At high CTAC concentrations, the CTA^+ ions adsorb on the hydrophilic and negative SiO_2 surface and assemble into "half micelles". Similar to the Si surface, the SiO_2 surface becomes positive after the CTAC adsorption. However, water molecules seep in between CTA^+ and SiO_2 because of the hydrophilicity of both particle surface and head group of CTA^+, resulting in a larger gap between the electrolyte and SiO_2.

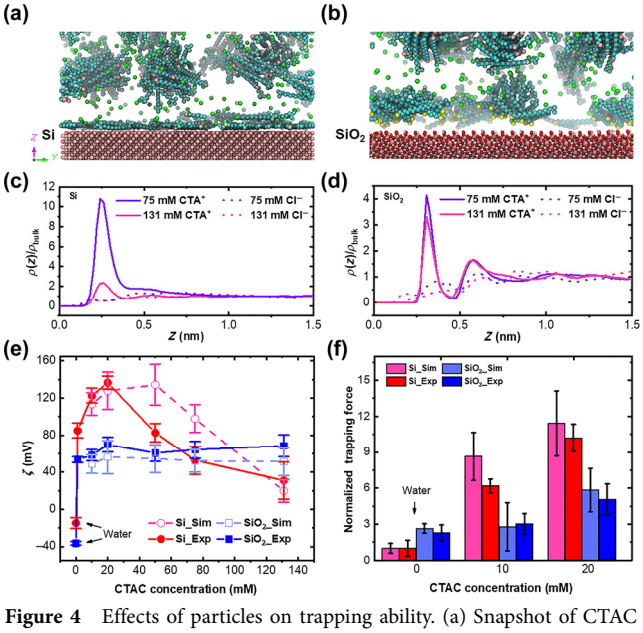

Figure 4 Effects of particles on trapping ability. (a) Snapshot of CTAC adsorption on the surface of Si particle. (b) Snapshot of CTAC adsorption on the surface of SiO_2 particle. Green, cyan, pink and yellow spheres are chlorine, carbon, carbon (tail) and nitrogen (head) atoms, respectively. In order to show a better comparison, water molecules are not plotted here (simulation setup is shown in Fig. S12 in the ESM). (c) Relative density profiles of adsorbed ions on the surface of Si particle in 75 and 131 mM CTAC solution. (d) Relative density profiles of adsorbed ions on the surface of SiO_2 particle in 75 and 131 mM CTAC solution. (e) Measured and simulated zeta potential of Si and SiO_2 particles in DI water and CTAC solution at various concentrations. (f) Measured and simulated normalized trapping force of Si and SiO_2 particles in DI water and CTAC solution at various concentrations. The sizes of Si and SiO_2 particles are 1 μm. Measured (simulated) trapping forces are normalized by dividing by the measured (simulated) trapping force of Si in DI water.

The relative interfacial ion densities, i.e. the ratio of ion density near the particle surface $\rho_{(Y)}$ to ion density in bulk solution ρ_{bulk} are summarized in Figs. 4(c) amd 4(d). For Si particles, a significant reduction of the relative density of CTA^+ can be observed when the concentration increases from 75 to 131 mM due to the saturating $\rho_{(Y)}$ and increased ρ_{bulk}. In contrast, the relative density of CTA^+ is almost constant for SiO_2 particles because both $\rho_{(Y)}$ and ρ_{bulk} increase simultaneously. It can be understood by the different working distance between two attraction forces, i.e. the working distance of electrostatic interactions is larger than that of hydrophobic interactions. For Si particles, the saturation of CTAC adsorption is reached at a much lower CTAC concentration because of short-range hydrophobic interaction. However, for SiO_2 particles, both $\rho_{(Y)}$ and ρ_{bulk} increase simultaneously when the CTAC concentration increases.

The measured and simulated zeta potentials of Si (red dots) and SiO_2 (blue squares) particles at different CTAC concentrations are also illustrated in Fig. 4(e) (see Method for the experimental details). A model comprising a modified Poisson-Boltzmann description is used to calculate zeta potentials [48]. An external electric field of 0.4 V/nm is applied along Y direction to generate the electroosmotic flow, as shown in Figs. 4(a) and 4(b). The zeta potential is calculated by

$$\zeta = -\frac{\eta v_z(0)}{\varepsilon_r \varepsilon_0 E_{external}} \tag{5}$$

where η is bulk viscosity, $v_z(0)$ is the fluid velocity at midpoint of the fluid layer (where the electrostatic potential is zero). We used the dielectric constant of SPC/E water, 68, as ε_r. Both the Si and SiO_2 particles are negative in DI water. The negative charge of Si particles arises from slight but inevitable oxidization during sample preparation. For Si particles, the measured zeta potential increases from 0 to 20 mM before adsorption saturation is reached and then decreases due to reduced CTAC adsorption at higher concentrations (Fig. 4(e)). Increased ρ_{bulk} effectively reduces Debye length, thus reducing ζ. Slightly different with experimental results, the simulated ζ of Si particles is higher when CTAC concentration is above 50 mM. This is because the oxidation of Si particles is neglected in MD simulations. The hydrogen doping (~ 10%) is also ignored in the Si model. For SiO_2 particles, ζ is saturated at around 10 mM and keeps constant till 130 mM, which is consistent with the constant relative CTA^+ density shown in Fig. 4(d). One should note that the maximum value of ζ_{Si} is higher than that of SiO_2 because of neutralization effect of CTA^+ by SiO^-.

To further validate our models, the optothermal trapping forces are simulated and compared with the experimental results, as summarized in Fig. 4(f). In order to reduce the computational cost in atomistic MD simulations, a temperature gradient of 20 K/nm is used in MD simulations, which is three orders of magnitude higher than the experimental values (~ 0.01 K/nm). This is widely used in thermoelectric and thermal energy transport fields, and a good match between simulations and experiments can be obtained [49–51]. Hydrodynamic drag force is measured to evaluate the thermoelectric force [52]

$$F = 3\pi\eta(T)dv\phi(h)$$
$$\phi(h) = \left[1 - \frac{9}{16}\left(\frac{d}{2h}\right) + \frac{1}{8}\left(\frac{d}{2h}\right)^3 - \frac{45}{256}\left(\frac{d}{2h}\right)^4 - \frac{1}{16}\left(\frac{d}{2h}\right)^5\right]^{-1} \tag{6}$$

where d is the diameter of the particle, h is particle-substrate distance and is calculated by subtracting the height of the focal plane of AuNIs substrate from that of the trapping particle, $\phi(h)$ is the correction factor of hydrodynamic boundary effect, v is mean drift velocity. The thermoelectric force is calculated by adding the net force (estimated according to the newton's second law) to the hydrodynamic drag force. Details are shown in Note S7 in the ESM. In this work, thermoelectric forces are evaluated in an electrostatic way [39]. In Ref. [39], $-(\psi_0/T)\nabla T(\varepsilon\zeta/\eta)$ defines the thermo-electrophoretic velocity, where $-(\psi_0/T)\nabla T$ represents the electrostatic field induced by temperature field, and $\varepsilon\zeta$ and $1/\eta$ correspond to the charge of particles and the Stokes drag coefficient, respectively. Herein, TE fields are also considered as electrostatic fields. Moreover, in this work, TE fields take account of the contribution of charge separation and water polarization at the atomistic level. The surface charge density is calculated by the zeta potential in Eq. (4) with the consideration of Debye length screening and particle size. The Stokes drag force is measured with the consideration of hydrodynamic boundary effect.

In DI water, measured and simulated trapping forces of Si particles are 0.035 pN and 0.051 μN , respectively. In CTAC solution, the trapping forces of both Si and SiO_2 particles increase monotonically with concentration from 0 to 20 mM, because of the increasing ζ and TE field. However, the trapping force on Si particle is larger than that of SiO_2 particle due to higher zeta-potential of Si particles. The trapping force on SiO_2 particles should be larger than that on Si particles in higher concentration CTAC solution, stemming from the constant ζ_{SiO2} and decreased ζ_{Si}.

5 Rational design of optothermal tweezers

In previous sections, we have clarified the mechanism of optothermal tweezers from the perspective of atomic-scale interaction. According to our understanding, we further implement the theoretical model to develop general design guidelines of optothermal tweezers for applications in life sciences and colloidal sciences: 1) Selection of electrolyte solution with large S_T difference between cations and anions can maximize the trapping force. DI water is also a good choice when the target objects own a highly negative surface charge. 2) Trapping force is usually strong in an electrolyte solution with the existence of micelles. 3) For hydrophobic particles, stable optothermal trapping can always be achieved in organic electrolyte solution. 4) For hydrophilic particles, trapping is achievable in an electrolyte solution (either organic or inorganic) when the TE field and particles' surface charge have the same sign.

Following the above guidelines, two types of new optothermal tweezers are developed. First, inorganic optothermal tweezers are designed by exchanging the Cl^- ions in NaCl solution with I^- to enhance ΔS_T [53] and improve the optothermal trapping force. Therefore, the mean drift velocity of positively charged PS in NaI solution is almost double of that in NaCl solution (Table 1 and Fig. 5). Thus, the more robust trapping can be achieved in NaI solution compared to NaCl solution. We design the second type of optothermal tweezers by exchanging the CTA^+ of CTAC solution into poly(diallyldimethylammonium) cations, i.e. $PDADMA^{n+}$ (molecular structure is shown in Fig. S8 in the ESM). Similar to CTA^+, $PDADMA^{n+}$ possesses a long and hydrophobic alkane chain. However, effective optothermal trapping of negative and positive particles can be achieved in poly(diallyldimethylammonium chloride) (PDADMAC) solution of ultralow concentration (0.1 μM). The remarkable TE field results from the larger S_T of $PDADMA^{n+}$. Specifically, for objects that are larger than Debye length [54],

$$S_T = \frac{D_T}{D} = \frac{4\pi R}{k_B T}\frac{\hat{h}}{T} \tag{7}$$

Table 1 A paramatric study of the performance of optothermal tweezers

Solution	Particles	Substrate	Power[a] (mW)	Drift velocity (μm/s)
NaI (10 mM)	Positive PS	AuNIs	0.05	1.47
NaCl (10 mM)	Positive PS	AuNIs	0.05	0.84
PDADMAC (0.1 μM)	Positive/ negative PS	AuNIs	0.05	0.38/ 0.43
CTAC (10 mM)	Positive/ negative PS	AuNIs	0.05	1.67/ 2.46
Water	Negative PS	AuNIs	0.05	1.57
Water	Negative silica	a:Si-H[56]	0.8	1.36
Water	Negative PS	Au nanostructure[57]	0.2	—
Tris (10 mM)	Negative DNA	PDMS[58]	10	—

[a]The optical powers of last three types of optothermal tweezers are their minimum values for stable trapping. The minimum power of the tweezers in this work can be as low as 0.02 mW.

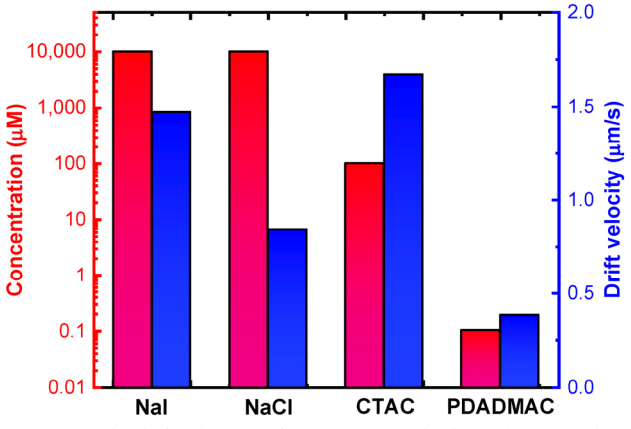

Figure 5 The drift velocities of a 2 μm positively charged PS particle in different solutions along with the corresponding electrolyte concentrations.

where R is the radius of the particle, k_B is Boltzmann constant, T is environment temperature, and $\hat{h}$ is solvation enthalpy density. PDADMA^{n+} possesses the larger size (molar mass: ~ 400,000) than that of CTA$^+$ micelles (molar mass: ~ 100,000). PDADMA^{n+} also has a higher enthalpy density since it contains n positive charges and has higher surface charge density than that of CTAC. Therefore, the intrinsic S_T of PDADMA^{n+} is larger. Additionally, in low-concentrated PDADMAC solution, $\Delta S_T^{coupling}$ between cations and anions becomes small (see Eq. (2)). The above-mentioned three factors guarantee a larger ΔS_T between PDADMA^{n+} and Cl$^-$ ions. Therefore, PDADMAC-based tweezers can reach the maximum trapping capability using lower-concentrated electrolytes (Fig. 5). Such optothermal tweezers can largely broaden their applications by reducing the limitations such as poor biocompatibility caused by high-concentrated electrolytes. Table 1 makes a comprehensive comparison between most reported types of optothermal tweezers with our novel tweezers (on the basis of NaCl, NaI, and PDADMAC solutions). The tweezers proposed in this work show superiorities in terms of working power, trapping strength and electrolyte concentration (Fig. 5). The trapping of particles in NaCl solution is reported for the first time to the best of our knowledge, though the repelling of particles has been reported before. Compared to water-based tweezers, NaCl/ NaI-based tweezers enable steady trapping of positively charged particles. Compared to CTAC-based tweezers, PDADMAC-based tweezers show steady trapping of both negative and positive particles at three orders of magnitude lower concentration. Beyond trapping, optothermal sorting of particles with different charges is also possible. For proof-of-concept, we demonstrate the optothermal sorting of positively charged PS particles and negatively charged SiO_2 particles in DI water (see Movie ESM7). Compared with sorting based on optical tweezers [55], opto-thermal sorting has higher throughput as optical tweezers are limited to a smaller focal area of the laser spot. Also, the low optical power intensity utilized in opto-thermal sorting reduces the damage to fragile objects. Moreover, optothermal sorting can also be applied to metallic particles and anisotropic particles that are difficult to trap by optical tweezers. There exists a size limitation for particles that can be trapped at the single-particle level by optothermal tweezers. The typical size range is from sub-100 nm to 9 μm . For a particle with smaller size, the trapping force is not big enough compared to Brownian motion. For a larger particle, the trapping force is too small to overcome friction forces. However, we could broaden the size range of trapped particles through substrate optimization or the use of an ultrafast laser.

6 Conclusions

By incorporating atomistic MD simulations with experiments, we have unraveled the underlying mechanism of optothermal trapping of micro-/nanoparticles, which involves the atomic-scale interactions among particle surface, solvent molecules and ionic species in the thermal field. We find that the TE field arising from charge separation and water polarization along the temperature gradient dominates the optothermal trapping. The surface properties of target particles such as surface charge and hydrophilicity dominate the particle-ion interactions and zeta potential of the particles. The Soret coefficients of ionic species in the solution determine the thermal response of ions along the temperature field, leading to a TE field generated by the spatial distribution of different ions. Our theoretical modeling is verified by systematically designed experiments. The atomistic models enable us to design new types of optothermal tweezers with low-concentrated electrolytes, strong trapping capability and enhanced biocompatiblity and to further demonstrate the optothermal sorting of the particle with different surface charges. With their expanded functionality and enhanced performance, these optothermal tweezers will find a wider range of applications in various areas.

7 Methods

7.1 Materials and sample preparation

Polystyrene beads (2 μm, Thermo Fisher Scientific) and silicon particles (1 μm, Bangs Laboratories) were purchased and redispersed in targeted liquid. The zeta potentials of the PS beads in DI water are −57.7 and 18.6 mV, respectively. CTAC, NaCl and PDADMAC were purchased from Sigma-Aldrich.

Au nanoisland substrate was prepared by depositing 4.5 nm Au thin films on glass slides by thermal deposition (Denton thermal evaporator, base pressure: 1×10^{-5} Torr) followed by thermal annealing at 550 °C for 2 h. The thickness of the Au films was chosen to maximize the absorption efficiency at the laser wavelength (532 nm). With a strong plasmonic absorption and heat localization after thermal annealing, AuNIs is cable of generating a highly localized thermal gradient field with laser radiation.

The synthesis protocols of the hydrogen-terminated amorphous

Si particles: Trisilane and n-hexane were added in a 10 mL titanium reactor placed in a nitrogen-filled glove box. The reactor (sealed) was taken out and heated to a certain temperature for 10 min for complete decomposition of trisilane. After the reaction, the reactor was cooled down to room temperature in an ice bath. The Si particles were then washed with chloroform by centrifuging at 8,000 rpm for 5 min. The size of the Si particles is decided by the amount of trisilane determines, while the reaction pressure is decided by the amount of n-hexane determines inside the reactor. The hydrogen concentration inside the Si particles was tuned by controlling the reaction temperatures. Note that the precipitate was collected and dispersed in chloroform before use to avoid oxidation.

7.2 Molecular dynamics simulation

All MD simulations were carried out with the LAMMPS package with the time step of 1 fs (for water and NaCl) or 0.25 fs (for CTAC) at 300 K and ambient pressure. Periodic boundary conditions were applied in all directions. The dimension of simulation boxes for water, NaCl and CTAC solutions are 3.4 nm × 5.2 nm × 25.9 nm. The rigid SPC/E model [59] was used for water molecules. Widely used TIP4P model [60] was also tested for comparison (Fig. S13 in the ESM). All-atom optimized potentials for liquid simulations (OPLS-AA) force field [61, 62] were used in all simulations. The partial charge and van der Waals (vdW) parameters of CTAC and NaCl were taken from Refs. [62, 63], respectively [63, 64]. The long-range electrostatic forces were computed with the P3M method. For all pairwise LJ terms, Lorentz-Berthelot mixing rule was applied. The cut-off distance in the LJ potential was set to 2.5σ. 300 ns non-equilibrium molecular dynamics (NEMD) simulations in the canonical ensemble were used to record simulation data after the structure relaxation in the isothermal–isobaric ensemble, followed by 1 ns microcanonical ensemble. Langevin thermostats were coupled with water molecules in the middle and boundaries of the system to generate temperature gradients. To obtain meaningful statistics, for each set of parameters, 12 independent simulations were performed. The setup of the MD simulations for zeta potential is slightly different: Periodic boundaries conditions were applied in X and Z axis and fixed boundary condition is applied in Y axis. The dimension of simulation boxes is 4.5 nm × 18.0 nm × 9.5 nm. The partial charge and vdW parameters of silicon and silica were taken from Refs. [64, 65].

7.3 Zeta potential measurement

Dynamic light scattering (DLS) measurements were performed through Malvern Zetasizer Nano ZS equipped with a 633 nm laser in backscattering configuration. Samples were loaded into a pre-rinsed folded capillary cell, and measurements were made at 25 °C, using an applied voltage of 150 V. For high concentration electrolyte solution, 40 V is used to avoid joule heating and electrode damage. Two samples were used to obtain averaged zeta potential. Three measurements were made for each sample.

Acknowledgements

The authors acknowledge the financial support of the National Science Foundation (No. NSF-CMMI-1761743), the National Aeronautics and Space Administration Early Career Faculty Award (No. 80NSSC17K0520), and the National Institute of General Medical Sciences of the National Institutes of Health (No. DP2GM128446). L. H. L. acknowledges financial support from the National Natural Science Foundation of China (No. 62075111) and the State Key Laboratory of Precision Measurement Technology and Instruments. The authors are grateful to Prof. Brian A. Korgel and Dr. Taizhi Jiang for providing Si particles. They also thank Yaoran Liu, Jingang Li, Kan Yao and Zhihan Chen for useful discussions.

Electronic Supplementary Material: Supplementary material (videos of opto-thermoeletric manipulation of particles, detailed investigation of TE fields and trapping forces, calculations of Soret coefficient, and measured zeta potentials) is available in the online version of this article at https://doi.org/10.1007/s12274-020-3087-z.

References

[1] Killian, J. L.; Ye, F.; Wang, M. D. Optical tweezers: A force to be reckoned with. *Cell* **2018**, *175*, 1445–1448.

[2] Zhang, P. R.; Chen, C. Y.; Guo, F.; Philippe, J.; Gu, Y. Y.; Tian, Z. H.; Bachman, H.; Ren, L. Q.; Yang, S. J.; Zhong, Z. W. et al. Contactless, programmable acoustofluidic manipulation of objects on water. *Lab Chip* **2019**, *19*, 3397–3404.

[3] Zhang, P. R.; Chen, C. Y.; Su, X. Y.; Mai, J.; Gu, Y. Y.; Tian, Z. H.; Zhu, H. D.; Zhong, Z. W.; Fu, H.; Yang, S. J. et al. Acoustic streaming vortices enable contactless, digital control of droplets. *Sci. Adv.* **2020**, *6*, eaba0606.

[4] Crane, M. J.; Pandres, E. P.; Davis, E. J.; Holmberg, V. C.; Pauzauskie, P. J. Optically oriented attachment of nanoscale metal-semiconductor heterostructures in organic solvents via photonic nanosoldering. *Nat. Commun.* **2019**, *10*, 4942.

[5] Ashkin, A.; Dziedzic, J. M.; Bjorkholm, J. E.; Chu, S. Observation of a single-beam gradient force optical trap for dielectric particles. *Opt. Lett.* **1986**, *11*, 288–290.

[6] Ilic, O.; Atwater, H. A. Self-stabilizing photonic levitation and propulsion of nanostructured macroscopic objects. *Nat. Photonics* **2019**, *13*, 289–295.

[7] Grier, D. G. A revolution in optical manipulation. *Nature* **2003**, *424*, 810–816.

[8] Rasmussen, M. B.; Oddershede, L. B.; Siegumfeldt, H. Optical tweezers cause physiological damage to *Escherichia coli* and *Listeria bacteria*. *Appl. Environ. Microbiol.* **2008**, *74*, 2441–2446.

[9] Babynina, A.; Fedoruk, M.; Kühler, P.; Meledin, A.; Döblinger, M.; Lohmuller, T. Bending gold nanorods with light. *Nano Lett.* **2016**, *16*, 6485–6490.

[10] Grigorenko, A. N.; Roberts, N. W.; Dickinson, M. R.; Zhang, Y. Nanometric optical tweezers based on nanostructured substrates. *Nat. Photonics* **2008**, *2*, 365–370.

[11] Zheng, Y. X.; Ryan, J.; Hansen, P.; Cheng, Y. T.; Lu, T. J.; Hesselink, L. Nano-optical conveyor belt, part II: Demonstration of handoff between near-field optical traps. *Nano Lett.* **2014**, *14*, 2971–2976.

[12] Lin, L. H.; Hill, E. H.; Peng, X. L.; Zheng, Y. B. Optothermal manipulations of colloidal particles and living cells. *Acc. Chem. Res.* **2018**, *51*, 1465–1474.

[13] Lin, L. H.; Wang, M. S.; Peng, X. L.; Lissek, E. N.; Mao, Z. M.; Scarabelli, L.; Adkins, E.; Coskun, S.; Unalan, H. E.; Korgel, B. A. et al. Opto-thermoelectric nanotweezers. *Nat. Photonics* **2018**, *12*, 195–201.

[14] Lin, L. H.; Zhang, J. L.; Peng, X. L.; Wu, Z. L.; Coughlan, A. C. H.; Mao, Z. M.; Bevan, M. A.; Zheng, Y. B. Opto-thermophoretic assembly of colloidal matter. *Sci. Adv.* **2017**, *3*, e1700458.

[15] Lin, L. H.; Peng, X. L.; Wei, X. L.; Mao, Z. M.; Xie, C.; Zheng, Y. B. Thermophoretic tweezers for low-power and versatile manipulation of biological cells. *ACS Nano* **2017**, *11*, 3147–3154.

[16] Hill, E. H.; Li, J. G.; Lin, L. H.; Liu, Y. R.; Zheng, Y. B. Opto-thermophoretic attraction, trapping, and dynamic manipulation of lipid vesicles. *Langmuir* **2018**, *34*, 13252–13262.

[17] Lin, L. H.; Peng, X. L.; Wang, M. S.; Scarabelli, L.; Mao, Z. M.; Liz-Marzan, L. M.; Becker, M. F.; Zheng, Y. B. Light-directed reversible assembly of plasmonic nanoparticles using plasmon-enhanced thermophoresis. *ACS Nano* **2016**, *10*, 9659–9668.

[18] Lin, L. H.; Peng, X. L.; Zheng, Y. B. Reconfigurable opto-thermoelectric printing of colloidal particles. *Chem. Commun.* **2017**, *53*, 7357–7360.

[19] Lin, L. H.; Kollipara, P. S.; Zheng, Y. B. Digital manufacturing of advanced materials: Challenges and perspective. *Mater. Today* **2019**, *28*, 49–62.
[20] Lin, L. H.; Lepeshov, S.; Krasnok, A.; Jiang, T. Z.; Peng, X. L.; Korgel, B. A.; Alù, A.; Zheng, Y. B. All-optical reconfigurable chiral meta-molecules. *Mater. Today* **2019**, *25*, 10–20.
[21] Brenner, H. Elementary kinematical model of thermal diffusion in liquids and gases. *Phys. Rev. E* **2006**, *74*, 036306.
[22] Lüsebrink, D.; Yang, M. C.; Ripoll, M. Thermophoresis of colloids by mesoscale simulations. *J. Phys. Condens Matter* **2012**, *24*, 284132.
[23] Putnam, S. A.; Cahill, D. G. Transport of nanoscale latex spheres in a temperature gradient. *Langmuir* **2005**, *21*, 5317–5323.
[24] Putnam, S. A.; Cahill, D. G.; Wong, G. C. L. Temperature dependence of thermodiffusion in aqueous suspensions of charged nanoparticles. *Langmuir* **2007**, *23*, 9221–9228.
[25] Bresme, F.; Hafskjold, B.; Wold, I. Nonequilibrium molecular dynamics study of heat conduction in ionic systems. *J. Phys. Chem.* **1996**, *100*, 1879–1888.
[26] Di Lecce, S.; Bresme, F. Thermal polarization of water influences the thermoelectric response of aqueous solutions. *J. Phys. Chem. B* **2018**, *122*, 1662–1668.
[27] Leaist, D. G.; Hao, L. Very large thermal separations for polyelectrolytes in salt solutions. *J. Chem. Soc., Faraday Trans.* **1994**, *90*, 1909–1911.
[28] Reichl, M.; Herzog, M.; Götz, A.; Braun, D. Why charged molecules move across a temperature gradient: The role of electric fields. *Phys. Rev. Lett.* **2014**, *112*, 198101.
[29] Würger, A. Transport in charged colloids driven by thermoelectricity. *Phys. Rev. Lett.* **2008**, *101*, 108302.
[30] Majee, A.; Würger, A. Thermocharge of a hot spot in an electrolyte solution. *Soft Matter* **2013**, *9*, 2145–2153.
[31] Vigolo, D.; Rusconi, R.; Stone, H. A.; Piazza, R. Thermophoresis: Microfluidics characterization and separation. *Soft Matter* **2010**, *6*, 3489–3493.
[32] Sehnem, A. L.; Figueiredo Neto, A. M.; Aquino, R.; Campos, A. F. C.; Tourinho, F. A.; Depeyrot, J. Temperature dependence of the Soret coefficient of ionic colloids. *Phys. Rev. E* **2015**, *92*, 042311.
[33] Liu, Y. R.; Lin, L. H.; Bangalore Rajeeva, B.; Jarrett, J. W.; Li, X. T.; Peng, X. L.; Kollipara, P.; Yao, K.; Akinwande, D.; Dunn, A. K. et al. Nanoradiator-mediated deterministic opto-thermoelectric manipulation. *ACS Nano* **2018**, *12*, 10383–10392.
[34] Lin, L. H.; Peng, X. L.; Mao, Z. M.; Wei, X. L.; Xie, C.; Zheng, Y. B. Interfacial-entropy-driven thermophoretic tweezers. *Lab Chip* **2017**, *17*, 3061–3070.
[35] Bresme, F.; Lervik, A.; Bedeaux, D.; Kjelstrup, S. Water polarization under thermal gradients. *Phys. Rev. Lett.* **2008**, *101*, 020602.
[36] Zhang, S. L.; Juvert, J.; Cooper, J. M.; Neale, S. L. Manipulating and assembling metallic beads with optoelectronic tweezers. *Sci. Rep.* **2016**, *6*, 32840.
[37] Witte, C.; Reboud, J.; Cooper, J. M.; Neale, S. L. Channel integrated optoelectronic tweezer chip for microfluidic particle manipulation. *J. Micromech. Microeng.* **2020**, *30*, 045004.
[38] Zhao, D.; Wang, H.; Khan, Z. U.; Chen, J. C.; Gabrielsson, R.; Jonsson, M. P.; Berggren, M.; Crispin, X. Ionic thermoelectric supercapacitors. *Energy Environ. Sci.* **2016**, *9*, 1450–1457.
[39] Würger, A. Thermal non-equilibrium transport in colloids. *Rep. Prog. Phys.* **2010**, *73*, 126601.
[40] Bregulla, A. P.; Würger, A.; Günther, K.; Mertig, M.; Cichos, F. Thermo-osmotic flow in thin films. *Phys. Rev. Lett.* **2016**, *116*, 188303.
[41] Gargiulo, J.; Brick, T.; Violi, I. L.; Herrera, F. C.; Shibanuma, T.; Albella, P.; Requejo, F. G.; Cortés, E.; Maier, S. A.; Stefani, F. D. Understanding and reducing photothermal forces for the fabrication of au nanoparticle dimers by optical printing. *Nano Lett.* **2017**, *17*, 5747–5755.
[42] Underwood, R.; Tomlinson-Phillips, J.; Ben-Amotz, D. Are long-chain alkanes hydrophilic? *J. Phys. Chem. B* **2010**, *114*, 8646–8651.
[43] Guthrie, G. Jr.; Wilson, J. N.; Schomaker, V. Theory of the thermal diffusion of electrolytes in a clusius column. *J. Chem. Phys.* **1949**, *17*, 310–313.
[44] Kollipara, P. S.; Lin, L. H; Zheng, Y. B. Thermo-electro-mechanics at individual particles in complex colloidal systems. *J. Phys. Chem. C* **2019**, *123*, 21639–21644.
[45] Ohsawa, K.; Murata, M.; Ohshima, H. Zeta potential and surface charge density of polystyrene-latex; comparison with synaptic vesicle and brush border membrane vesicle. *Colloid Polym. Sci.* **1986**, *264*, 1005–1009.
[46] Scales, P. J.; Grieser, F.; Healy, T. W.; White, L. R.; Chan, D. Y. C. Electrokinetics of the silica-solution interface: A flat plate streaming potential study. *Langmuir* **1992**, *8*, 965–974.
[47] Williams, R.; Goodman, A. M. Wetting of thin layers of SiO_2 by water. *Appl. Phys. Lett.* **1974**, *25*, 531–532.
[48] Huang, D. M.; Cottin-Bizonne, C.; Ybert, C.; Bocquet, L. Ion-specific anomalous electrokinetic effects in hydrophobic nanochannels. *Phys. Rev. Lett.* **2007**, *98*, 177801.
[49] Römer, F.; Wang, Z. L.; Wiegand, S.; Bresme, F. Alkali halide solutions under thermal gradients: Soret coefficients and heat transfer mechanisms. *J. Phys. Chem. B* **2013**, *117*, 8209–8222.
[50] Wang, H. D.; Hu, S. Q.; Takahashi, K.; Zhang, X.; Takamatsu, H.; Chen, J. Experimental study of thermal rectification in suspended monolayer graphene. *Nat. Commun.* **2017**, *8*, 15843.
[51] Ma, D. K.; Ding, H. R.; Wang, X. M.; Yang, N.; Zhang, X. The unexpected thermal conductivity from graphene disk, carbon nanocone to carbon nanotube. *Int. J. Heat Mass Transfer* **2017**, *108*, 940–944.
[52] Faxen, H. Die bewegung einer starren kugel langs der achse eines mit zaher flussigkeit gefullten rohres. *Ark. Mat., Astron. Fys.* **1923**, *17*, 1–28.
[53] Takeyama, N.; Nakashima, K. Proportionality of intrinsic heat of transport to standard entropy of hydration for aqueous ions. *J. Solution Chem.* **1988**, *17*, 305–325.
[54] Würger, A. Is Soret equilibrium a non-equilibrium effect? *Comptes Rendus Mécanique* **2013**, *341*, 438–448.
[55] MacDonald, M. P.; Spalding, G. C.; Dholakia, K. Microfluidic sorting in an optical lattice. *Nature* **2003**, *426*, 421–424.
[56] Flores-Flores, E.; Torres-Hurtado, S. A.; Páez, R.; Ruiz, U.; Beltrán-Pérez, G.; Neale, S. L.; Ramirez-San-Juan, J. C.; Ramos-Garcia, R. Trapping and manipulation of microparticles using laser-induced convection currents and photophoresis. *Biomed. Opt. Express* **2015**, *6*, 4079–4087.
[57] Chen, J. J.; Kang, Z. W.; Kong, S. K.; Ho, H. P. Plasmonic random nanostructures on fiber tip for trapping live cells and colloidal particles. *Opt. Lett.* **2015**, *40*, 3926–3929.
[58] Braun, D.; Libchaber, A. Trapping of DNA by thermophoretic depletion and convection. *Phys. Rev. Lett.* **2002**, *89*, 188103.
[59] Berendsen, H. J. C.; Grigera, J. R.; Straatsma, T. P. The missing term in effective pair potentials. *J. Phys. Chem.* **1987**, *91*, 6269–6271.
[60] Ding, H. R.; Peng, G. L.; Mo, S. Q.; Ma, D. K.; Sharshir, S. W.; Yang, N. Ultra-fast vapor generation by a graphene nano-ratchet: A theoretical and simulation study. *Nanoscale* **2017**, *9*, 19066–19072.
[61] Cornell, W. D.; Cieplak, P.; Bayly, C. I.; Gould, I. R.; Merz, K. M.; Ferguson, D. M.; Spellmeyer, D. C.; Fox, T.; Caldwell, J. W.; Kollman, P. A. A second generation force field for the simulation of proteins, nucleic acids, and organic molecules. *J. Am. Chem. Soc.* **1995**, *117*, 5179–5197.
[62] Sui, X.; Ding, H. R.; Yuan, Z. W.; Leong, C. F.; Goh, K.; Li, W.; Yang, N.; D'Alessandro, D. M.; Chen, Y. The roles of metal-organic frameworks in modulating water permeability of graphene oxide-based carbon membranes. *Carbon* **2019**, *148*, 277–289.
[63] Pal, S.; Bagchi, B.; Balasubramanian, S. Hydration layer of a cationic micelle, C_{10}TAB: Structure, rigidity, slow reorientation, hydrogen bond lifetime, and solvation dynamics. *J. Phys. Chem. B* **2005**, *109*, 12879–12890.
[64] Smith, D. E.; Dang, L. X. Computer simulations of NaCl association in polarizable water. *J. Chem. Phys.* **1994**, *100*, 3757–3766.
[65] Chai, J. C.; Liu, S. Y.; Yang, X. N. Molecular dynamics simulation of wetting on modified amorphous silica surface. *Appl. Surf. Sci.* **2009**, *255*, 9078–9084.